Interface engineering for high-efficiency spin injection and polarized emission in GaN-based devices

Qihong Lai [1], Weilin Hu [1], Mingyu Chen [1], Hongshu Li [1], Ying Ye [1], Guimin Liao [1], Jian Huang [1], Xuanli Zheng[1], Lijing Kong[1], Yaping Wu[1,†], Xu Li[1,†], Zhiming Wu[1,†] and Junyong Kang[1]

[1] Department of Physics, Engineering Research Center for Micro-Nano Optoelectronic Materials and Devices of Ministry of Education, OSED, Fujian Provincial Key Laboratory of Semiconductor Materials and Applications, Xiamen University, Xiamen 361005, People's Republic of China

[†] Correspondence to: Yaping Wu, Email: ypwu@xmu.edu.cn (Corresponding author)
Xu Li, Email: xuliphys@xmu.edu.cn (Corresponding author)
Zhiming Wu, Email: zmwu@xmu.edu.cn (Corresponding author)

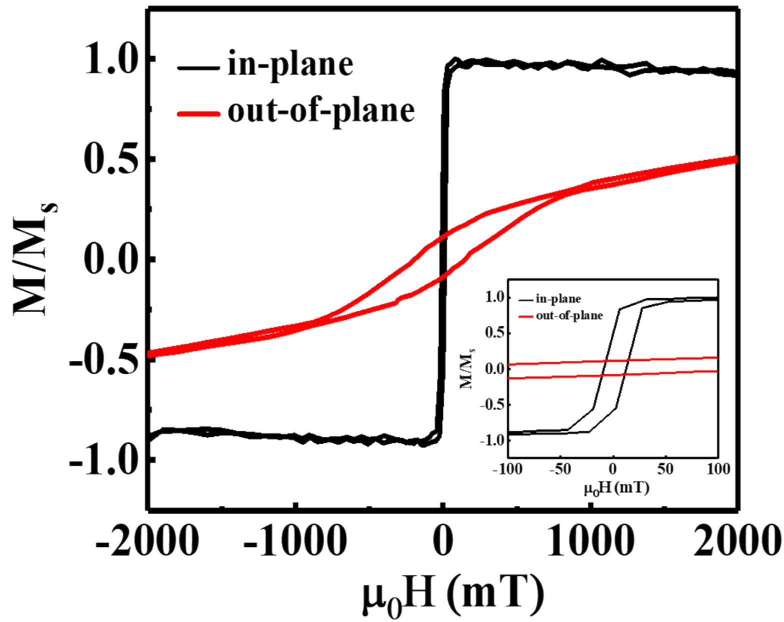

Fig. S1. (Color online) Room-temperature magnetic hysteresis loops of the annealed CoFeB film. The black curve corresponds to the in-plane hysteresis loop, and the red curve corresponds to the out-of-plane hysteresis loop. The inset shows an enlarged view of the low-field region to highlight the loop details near zero field.

Fig. S1 shows the magnetic hysteresis loops of the annealed CoFeB film. The hysteresis loop for in-plane magnetization exhibits a square-shaped profile, indicating that the easy magnetization direction of the material is oriented in the in-plane direction, with a coercivity of approximately 15 mT and a saturation magnetization field of about 50 mT.

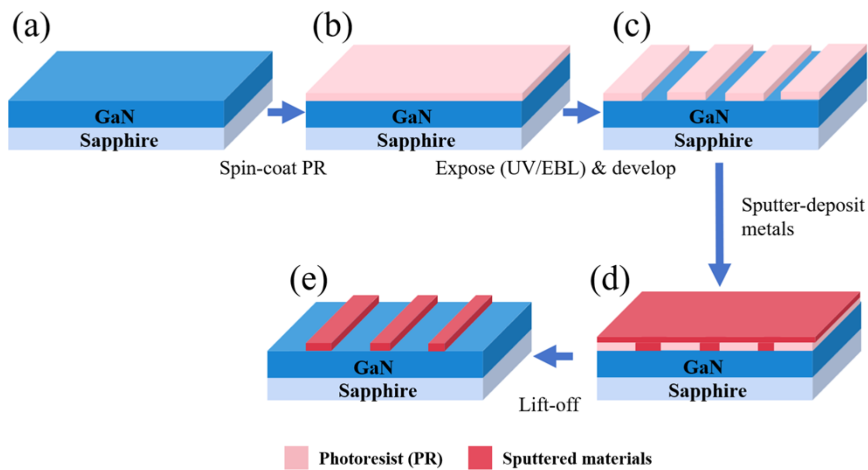

Fig. S2. (Color online) Schematic illustration of the fabrication process for the three-terminal Device I and the four-terminal MgO-junction device.

Fig. S2 schematically illustrates the fabrication process of Device I and the four-terminal CoFeB/MgO/GaN device. First, a photoresist was spin-coated on the GaN substrate and patterned by exposure and development according to the device layout, where UV photolithography was used for Device I and electron-beam lithography (EBL) was used for the four-terminal device. Subsequently, MgO/CoFeB/Ru layers were sequentially deposited by magnetron sputtering, followed by lift-off to remove the excess films, thereby yielding the complete device structure.

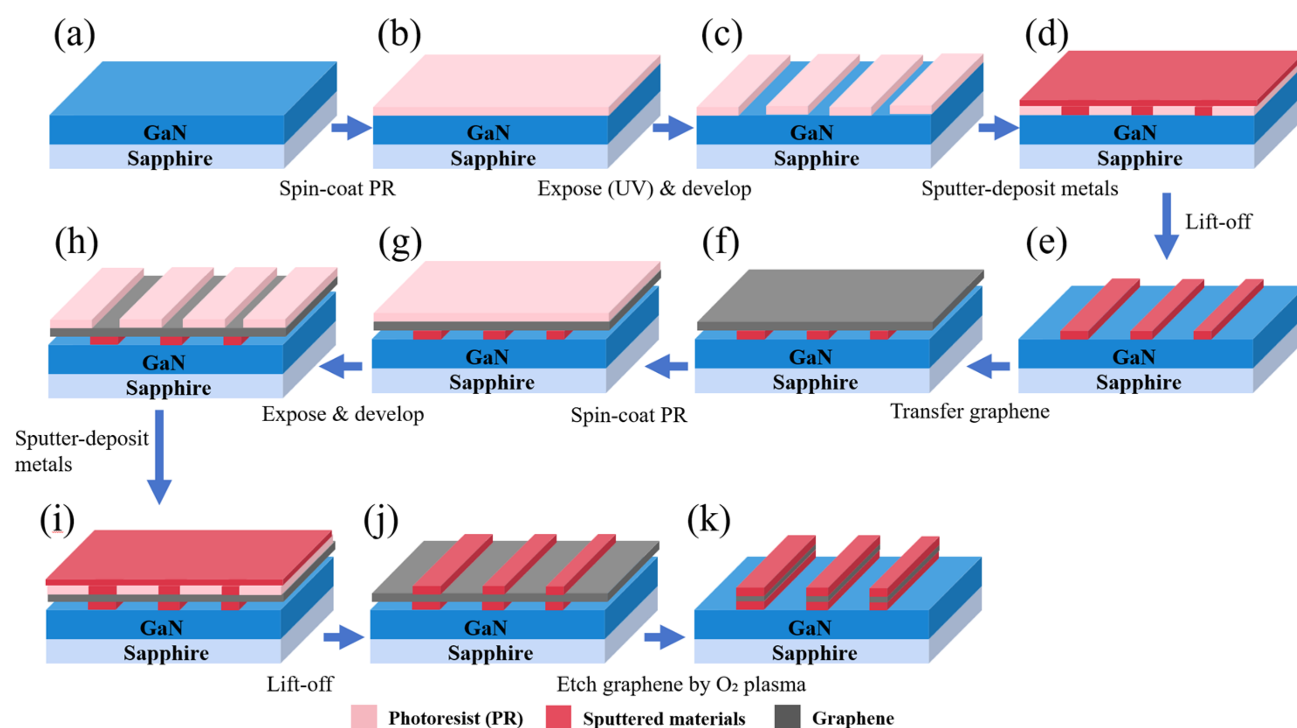

Fig. S3. (Color online) Schematic illustration of the fabrication process for the three-terminal Device II.

Fig. S3 schematically illustrates the fabrication process of Device II. First, a photoresist was spin-coated on the GaN substrate and patterned by exposure and development according to the device layout. The first layer (MgO) was then deposited, followed by lift-off to define the first thin-film structure. Subsequently, monolayer graphene was transferred onto the target substrate. The sample then underwent a second lithography cycle, in which the photoresist was spin-coated again, patterned by exposure and development, and followed by CoFeB/Ru deposition and lift-off to form the electrodes. Finally, oxygen plasma etching was used to remove graphene in the exposed regions while preserving the graphene beneath the electrodes/channel, yielding the final device structure.

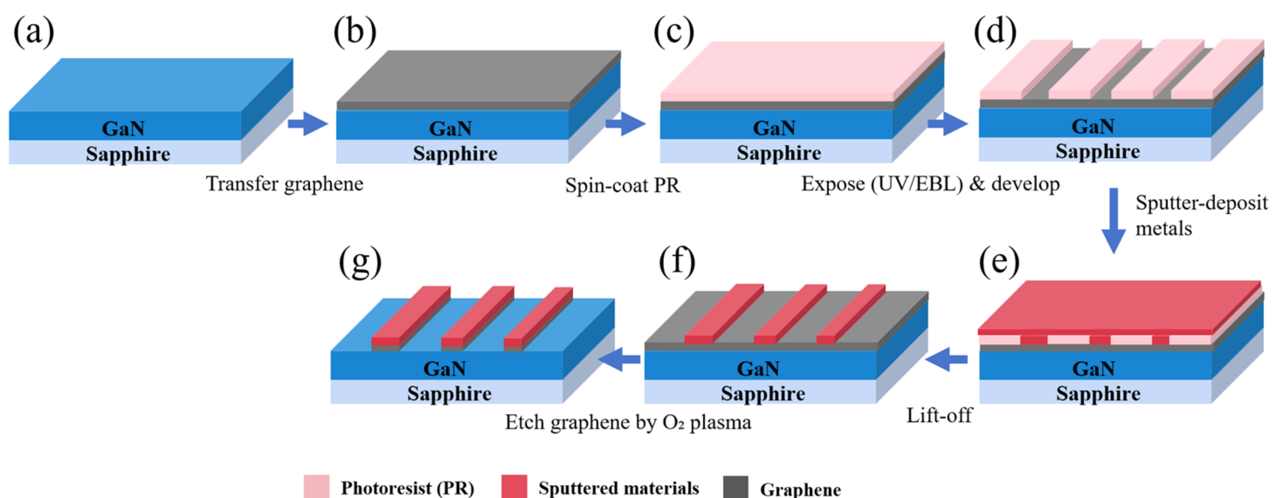

Fig. S4. (Color online) Schematic illustration of the fabrication process for the three-terminal Device III and the four-terminal MgO/Graphene-junction device.

Fig. S4 schematically illustrates the fabrication process of the three-terminal Device III and the four-terminal CoFeB/MgO/Graphene/GaN device. First, monolayer graphene was transferred onto the GaN substrate surface. A photoresist was then spin-coated and patterned by exposure and development according to the device layout, where UV photolithography was used for the three-terminal device and electron-beam lithography (EBL) was used for the four-terminal device. After patterning, MgO/CoFeB/Ru layers were sequentially deposited by magnetron sputtering, followed by lift-off to remove the excess films, thereby forming the complete electrode/stack structure. Finally, oxygen plasma etching was used to remove graphene in the exposed regions while preserving the graphene beneath the electrodes/channel, yielding the final device structure.

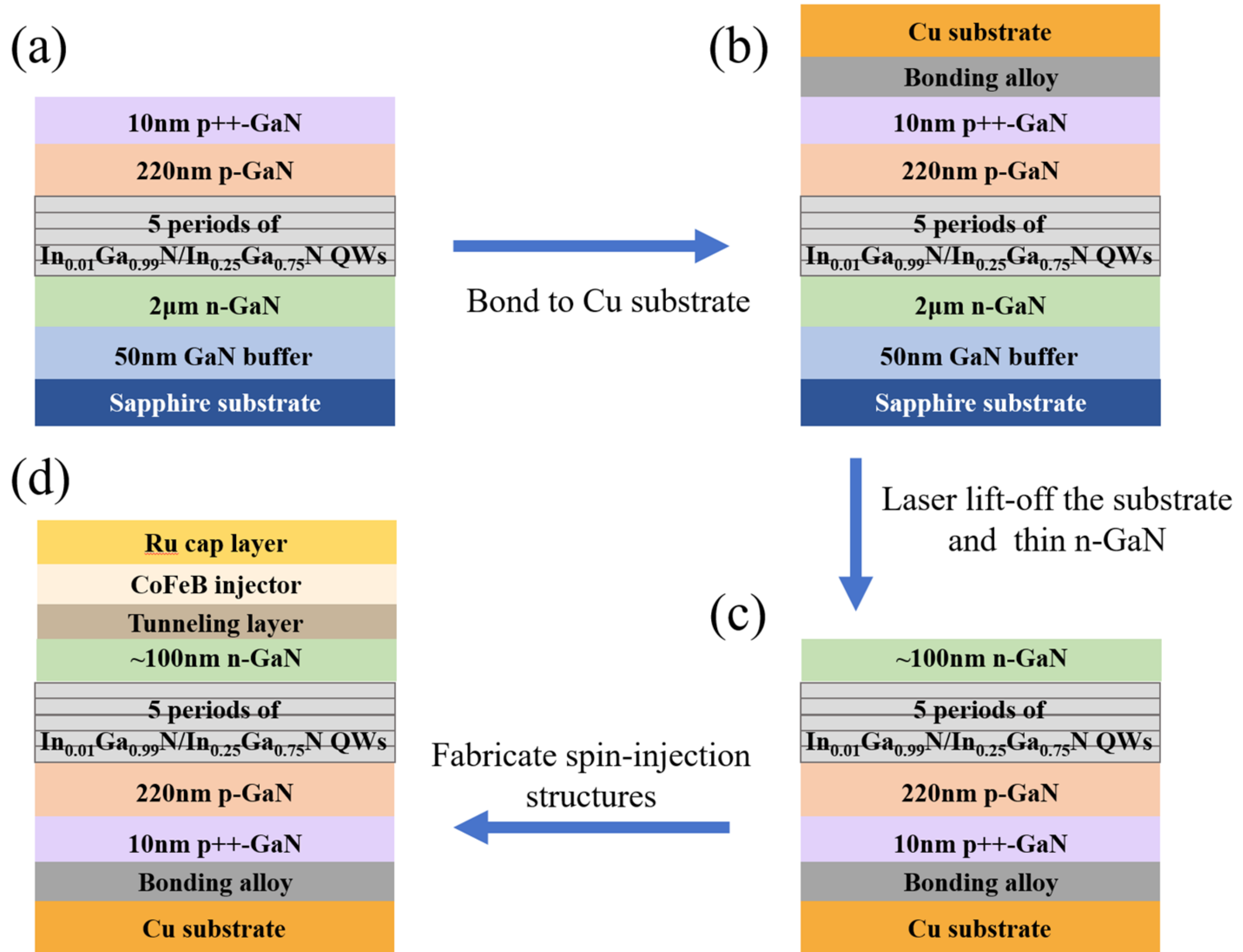

Fig. S5. (Color online) Schematic illustration of the structure and key fabrication steps of the inverted (flip-chip) spin-LED.

Fig. S5 summarizes the key fabrication process of the flip-chip spin-LED. While maintaining the epitaxial quality of the conventional p-i-n structure, the wafer is bonded and flipped, and the original substrate is removed so that the n-GaN transport layer becomes the top surface of the device. The n-GaN layer is then thinned by ICP etching to ~100 nm, in order to shorten the transport path of spin-polarized electrons before radiative recombination and to suppress potential spin-scattering losses. On this thinned n-GaN surface, the spin-injection structure is subsequently fabricated, enabling spin-polarized electrons to be injected from the n side and to recombine radiatively in the quantum-well region.

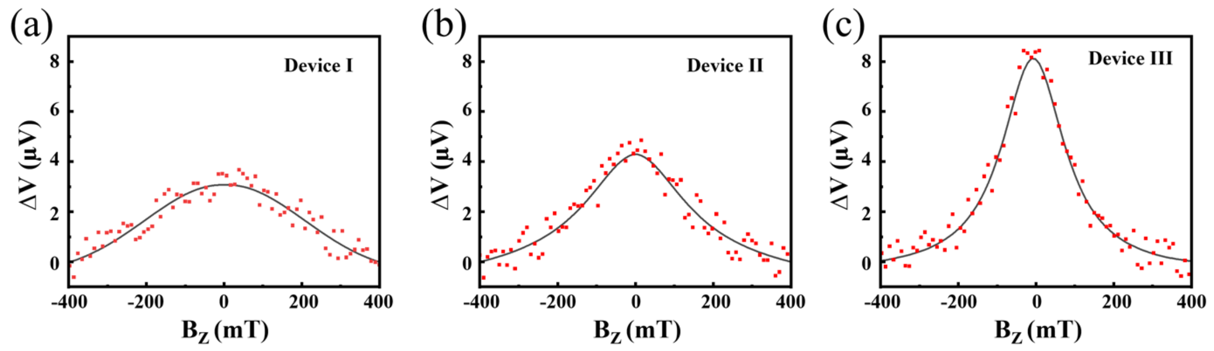

Fig. S6. (Color online) Hanle signals of the different three-terminal devices at an injection current of 5.0 μA. The scattered points represent the experimental data, and the solid lines are the fitted curves.

Fig. S6(a)−S6(c) present the raw Hanle data and Lorentzian fitted curves for Devices I, II, III at an injection current of 5.0 μA, respectively. Based on the fitted curves, the spin relaxation times τ_s for the different devices are determined to be 18 ± 3 ps (Device I), 34 ± 3 ps (Device II), and 60 ± 3 ps (Device III). Utilizing the spin diffusion relation, the corresponding spin diffusion lengths λ_s are calculated as 95 ± 7 nm (Device I), 133 ± 5 nm (Device II), and 175 ± 4 nm (Device III).

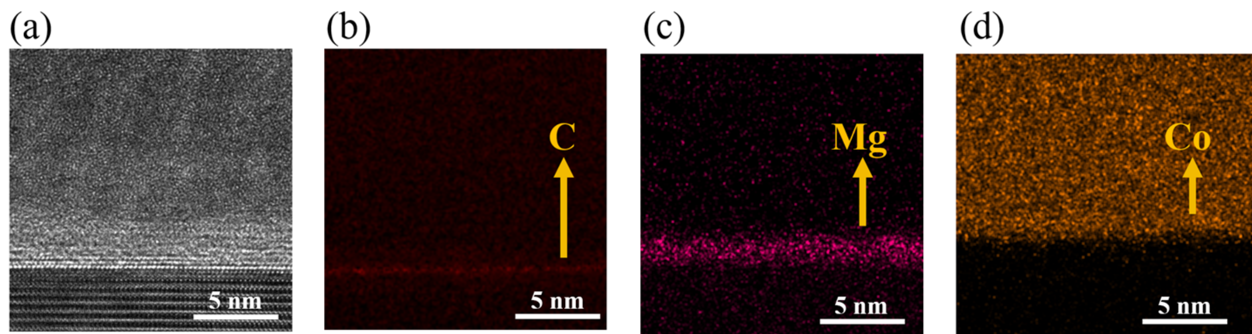

Fig. S7. (Color online) TEM image and the corresponding EDS elemental maps. (a) TEM image of the CoFeB/MgO/Graphene/GaN interface in the target interfacial region. (b)−(d) EDS elemental maps of (b) C, (c) Mg, and (d) Co.

Fig. S7 presents the cross-sectional TEM image of the CoFeB/MgO/Graphene/GaN interface together with the corresponding EDS elemental maps of C, Mg, and Co. As shown in Fig. S7(b), a localized, band-like C-rich signal is observed at the MgO/GaN interface; this signal is located between the MgO-enriched region and the underlying GaN (see Fig. S7(c)). Meanwhile, the Mg and Co signals are largely confined to their respective layers (Figs. S7(c) and S7(d)). Combined with the cross-sectional TEM morphology (Fig. S7(a)), the observed band-like C signal is consistent with the

designed position of the graphene interlayer, providing additional evidence for the presence of graphene at the interface.

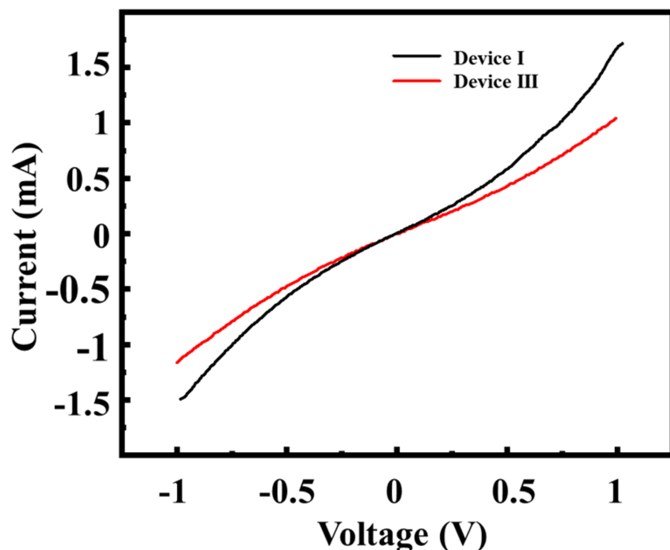

Fig. S8. (Color online) The I-V characteristics of Device I and Device III.

Fig. S8 presents the I-V curves of Devices I and III. Both curves exhibit distinct nonlinear characteristics, with slow current variation in the low-bias region and a rapid current rise as the bias increases, which reflects a non-ohmic transport behavior. Compared with Device I, Device III shows a generally lower current at the same applied bias, indicating that the insertion of graphene results in a significant reduction in electrical conductance and an increase in the barrier height.

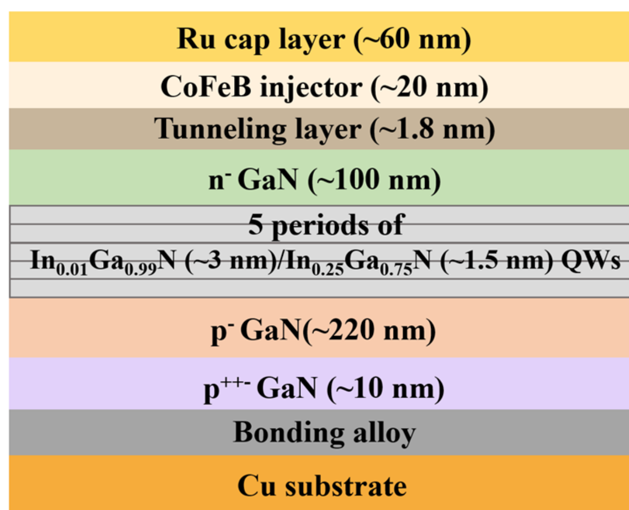

Fig. S9. (Color online) Schematic illustration of the layer structure of the inverted spin-LED.

Fig. S9 shows the layer structure of the device, consisting of a Ru capping layer, a CoFeB spin injector, a tunneling layer (MgO or MgO/Graphene), ~100 nm n-GaN, a 5-period $In_{0.01}Ga_{0.99}N$ (~3 nm)/ $In_{0.25}Ga_{0.75}N$ (~1.5 nm) quantum-well active region, 220 nm p-GaN, 10 nm p++-GaN, a bonding layer, and a Cu substrate. In this flip-chip configuration, the spin-injection stack is located on the n-side, enabling the injection of spin-polarized carriers through the tunnel barrier and their subsequent radiative recombination in the quantum wells.

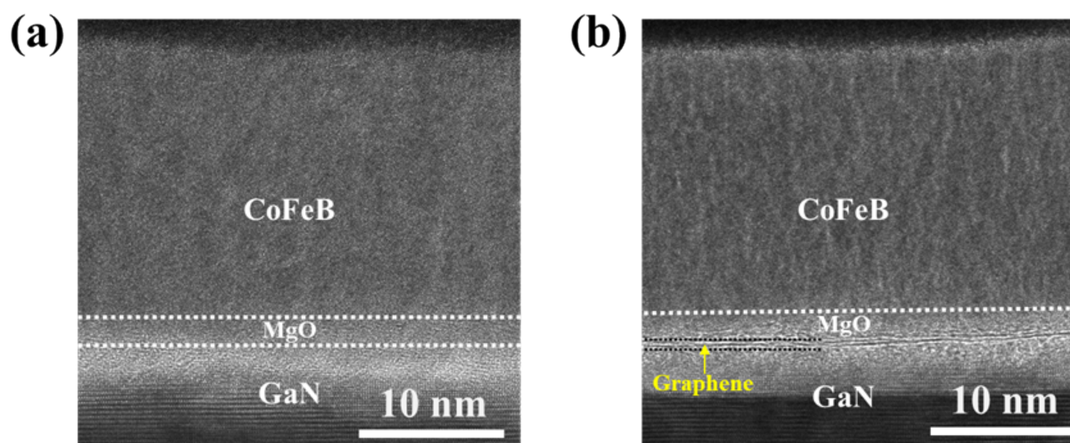

Fig. S10. (Color online) Cross-sectional TEM images of the injection interfaces in flip-chip spin-LEDs (a) without graphene and (b) with graphene insertion.

Fig. S10 presents the cross-sectional TEM images of the injection interfaces in flip-chip spin-LEDs with and without graphene insertion. The TEM results indicate that, after ICP etching, a thin amorphous layer with a thickness of ~ 2 nm is formed on top of the GaN surface. This is the main difference in the injection interface between the flip-chip spin-LEDs and the planar three-terminal and four-terminal devices. For the sample without graphene, as shown in Fig. S10(a), MgO is in direct contact with this amorphous GaN layer. Such direct contact is expected to introduce stronger structural disorder and more complicated local interfacial coupling, thereby giving rise to more interface-related scattering and becoming unfavorable for the preservation of spin polarization during injection. This is also consistent with the fact that the circular polarization obtained in the spin-LED is lower than the spin injection efficiency extracted from the planar transport devices. In contrast, for the graphene-inserted sample shown in Fig. S10(b), graphene can be clearly observed between MgO and the GaN, effectively separating the two materials and forming a clearer MgO/graphene/GaN transition interface. This result indicates that, even on the rough surface produced by ICP etching, graphene can still serve as an effective buffer and decoupling layer at the actual injection interface, weakening the direct

coupling between MgO and the GaN, helping preserve a better-defined tunneling interface, and thereby suppressing interface-related scattering. In addition, the slight undulation and local projection overlap of graphene in Fig. S10(b) suggest that monolayer graphene retains a certain degree of conformal adaptability on the rough interface, further supporting its buffering and interfacial regulating role within the local contact region. Correspondingly, the graphene-inserted spin-LED exhibits a higher circular polarization than the device without graphene. Although the actual injection interface in the flip-chip spin-LED is more complex than that in the planar three-terminal and four-terminal devices due to the ICP-induced damaged layer, the supplemented TEM results demonstrate that graphene still improves the effective spin injection mainly by optimizing the injection interface, weakening the direct coupling between MgO and the damaged GaN surface, and suppressing interface-related scattering. This role is consistent in direction with the interfacial engineering mechanism proposed for the planar devices.

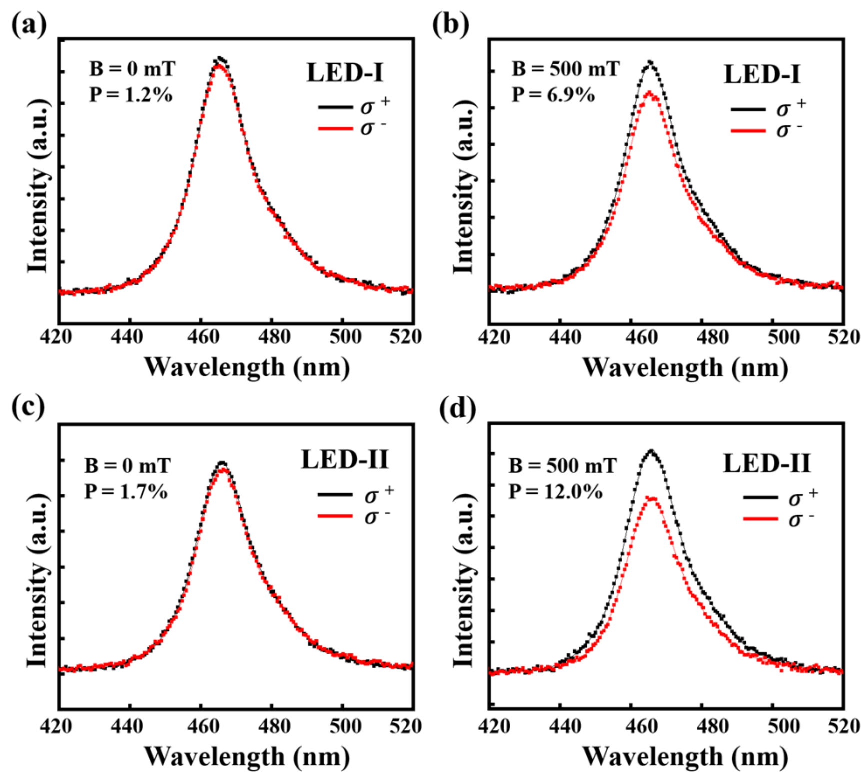

Fig. S11. (Color online) Spin-resolved electroluminescence spectra emitted from the surface of spin-LEDs. (a) and (b) Emission spectra of LED-I at 0 and 500 mT, respectively. (c) and (d) Emission spectra of LED-II at 0 and 500 mT, respectively. The symbols represent the raw experimental data, and the solid lines represent the corresponding smoothed curves for visual guidance. The working current is 2 mA, and the applied magnetic field is perpendicular to the surface of LED.

Fig. S11 presents the spin-resolved surface-emission spectra of LED-I and LED-II under an out-

of-plane magnetic field. In the absence of an external magnetic field, the circular polarization ratio of LED-I and LED-II is 1.2% and 1.7%, respectively. After applying a 500 mT out-of-plane magnetic field, their circular polarization ratios increase to 6.9% and 12.0%, respectively. It is evident that the circular polarization of LED-II consistently exceeds that of LED-I, indicating that the CoFeB/MgO/Graphene tunnel junctions exhibit a higher spin injection efficiency. Additionally, it should be noted that the devices exhibit a higher circular polarization for edge-emission than for surface emission in this work, which is associated with the magnetic anisotropy of the ferromagnetic materials. For the ferromagnetic materials employed in this work, the easy magnetization axis is oriented along the in-plane direction (see Fig. S1). Thus, a high magnetic field (1000 mT) is required for surface-emission measurements to achieve magnetic saturation of the ferromagnetic layer, and thus obtain a high circular polarization ratio. However, the applied out-of-plane magnetic field strength in this work is limited to only 500 mT, which prevents the magnetic moments of the ferromagnetic layer from reaching saturation. This consequently results in an overall lower circular polarization ratio for surface emission.